2021

Scale model behaviour and float geometry influence on an oscillating water column system

Cresswell, D.

Cresswell, D. (2021) 'Scale model behaviour and float geometry influence on an oscillating water column system', The Plymouth Student Scientist, 14(2), pp. 279-310.
http://hdl.handle.net/10026.1/18507

The Plymouth Student Scientist
University of Plymouth

*The Plymouth Student Scientist, 2021, **14**, (2), 279-310*

Scale model behaviour and float geometry influence on an oscillating water column wave energy device

Daniel Cresswell

Project Advisor: Dr. Keri Collins, School of Engineering, Computing & Mathematics, University of Plymouth, Drake Circus, Plymouth, PL4 8AA

Abstract

A numerical model based on a 1:60 scale Lazy-S Mooring Line has been developed using the dynamic analysis software OrcaFlex, to determine the software's capabilities when analysing discretized scale models, and to quantify the effect that varying float surface geometry has on mooring line system damping. Static analysis was performed, followed by dynamic analysis, based on experimental data from physical testing in the University of Plymouth 35m Sediment Flume tank, against two distinct float shapes with equivalent hydrostatic properties but aspect ratio variance perpendicular to fluid flow. The impact of scale modelling on static line forces, effective tension and driving frequency were evaluated as a comparative base between the experimental and numerical findings, and the intricacies of scale modelling evaluated in the context of the OrcaFlex software.

Evaluation of Static Line Forces (SLF) finds that systems comprised of taut lines at scale can misinterpret line tension as constant and may not exhibit expected static and dynamic tension behaviour, theorized as due to the nodal method OrcaFlex adopts for calculating line tension. Dynamic analysis of driving frequency amplitude suggests an agreement of behaviour between data sets – i.e, a reduced surface area results in a greater driving frequency of tension loading, particularly in the Heave direction of Oscillating Water Column (OWC) motion – based on the original defined float types and a proposed plate of 30% greater drag area. Drag area was determined to have a reduced influence at higher frequencies due to motion lag within the system such that, as OWC motion scales past a certain threshold, optimisation of float geometry will yield diminishing returns.

Consequently, evaluation of results suggests that numerical scale modelling in OrcaFlex is an appropriate method for modelling behaviour as a function of changing hydrostatic properties, but that consideration must be made when modelling taut scale systems to limit potential numerical discrepancies.

Keywords: OrcaFlex, scale modelling, numerical modelling, hydrodynamics, mooring lines, buoyancy module, float, OWC, oscillating water column, shallow water, Lazy-S, Heave, Surge

Introduction

With the acceleration toward low-carbon economies, the demand for alternative, sustainable energy sources is growing (*Tullow Oil Annual Report*, 2019). Although wind energy continues to provide the largest contribution to renewables growth at the time of writing (Giorgi, Gomes & Henriques, 2020), alternative solutions to the global energy crisis have been proposed in the form of extensively studied Wave Energy Conversion (WEC) devices utilizing Lazy-S mooring system designs.

The analysis of mooring line performance is paramount for the success of the OWC system, as improper application can have serious implications in terms of efficiency of energy conversion, their lifetime cost and the protection of in-field assets(Martinelli & Zanuttigh, 2018). Cost as a function of performance must be optimised, particularly as the sector of wave energy attracts investors and potential shareholders that may understandably be concerned as to the profitability of technological advancement.

This investigation evaluates a WEC Oscillating Water Column (OWC) Lazy-S mooring system at 1:60 scale, with an emphasis on hydrodynamic variation as a result of varying float area perpendicular to fluid flow. The evaluation is carried out through numerical modelling in the dynamic analysis software *OrcaFlex*, which is typically used for developing full-scale models (Paduano, Giorgi & Gomes, 2020). Evaluations of scale models in *OrcaFlex* are rare, granted that industrial application requires the fulfilment of standards proposed for as-built systems (DNV-GL, 2010). Subsequently, study of scale dynamics against experimental data is a unique opportunity that may provide insight as to the accuracy of numerical software modelling.

Oscillating Water Column

The research of Roberts (2020) and Scott (2020) into Lazy-S mooring line performance was developed in the context of an Oscillating Water Column (OWC) system first proposed by Collins, Howey and Greaves (2018). Oscillating Water Column WEC devices consist of a partially submerged reservoir with a water column (open to the sea below the waterline) and column of trapped air, which rarefies and pressurises to rotate a PTO turbine system (Kisacik, Stratigaki & Wu, 2020). The principal motion of an OWC device acts through the *Surge* and *Heave* directions of motion.

The mooring line plays a significant role in the performance of an OWC, particularly with recent trends toward deep-water OWC sites (Bingham *et al.*, 2015) which reduce shoaling energy losses (O'Connell, Cashman & Thiebaut, 2017). DNV-GL (2010), an industry standard regulatory body, recommend hydrodynamic performance evaluation of floating structures under 1-year, 5-year and 100-year environmental extremes, enhancing the need for stringent mooring line systems and optimisation that can counter the effects of deep-water installations (Ali & Hwa, 2020).

Mooring Lines

A mooring systems' impact on cost of energy for an OWC is estimated to be around 10% of the capital expenditure (CAPEX) and can provide up to 80% of total damping (Huse, 1991). Application of a mooring system facilitates a floating structure's ability to station-keep through lateral restoring forces (Davidson & Ringwood, 2017), attributed primarily to the elastic stretching resistance of taut lines or the submerged weight of suspended mooring chain. A typical Lazy-S mooring system is comprised as given in Figure 1.

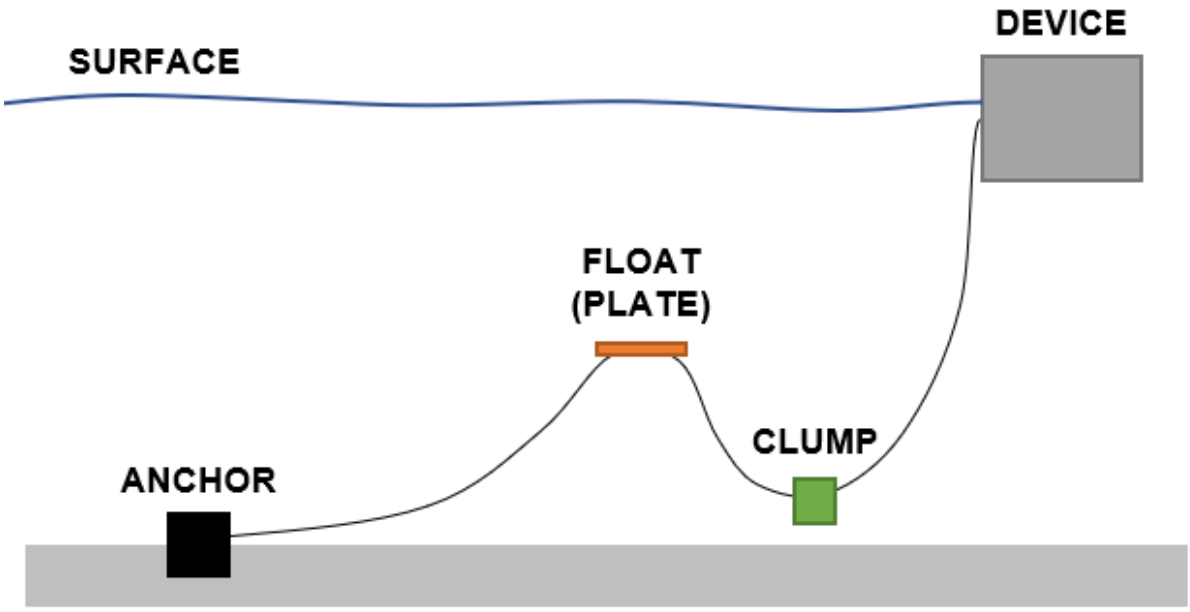

Figure 1: Lazy-S Mooring System Diagram

As the submerged mooring line acts to restrict the OWC device, significant fluid drag acts on the submerged components. Resultantly, the drag occurrence on a Lazy-S buoyancy module can change the hydrodynamics, and in some instances increase the probability of snap loading (Palm and Eskilsson, 2019) detectable during device heave motion (Touzon, 2020). Damping of motion in energy generation, excessive line loads and system energy losses can also be attributed to improper float geometry (Roberts, 2020), which can have severe consequences depending on the device's intended purpose.

Roberts & Scott Study (2020)

The foundations of this study are two collaborative investigations into hydrodynamic Lazy-S mooring line performance, as a function of buoyancy module aspect ratio, performed by George Roberts (2020) and Benjamin Scott (2020). The 1:60 scale model of a Lazy-S mooring line was developed and evaluated with three distinct floats – spar, cylinder and plate – under actuated motion in surge and heave, with properties given in Table 1. The recorded experimental data allows for the development of a numerical model in OrcaFlex and comparison to determine equivalence. Note that the drag forces are estimated based on geometry, rather than a current velocity present in the flume tank, and that the range of geometry was selected to elicit the greatest variation of hydrodynamics between each buoyancy module.

Table 1: Buoyancy Module Geometry Properties

Geometry	Flow Velocity (m/s)	Drag Coefficent	Surface Area (mm^2)	Drag Force (N)	Buoyancy Force (N)
Plate	0.124	1.28	5490.81	0.00543	0.3817
Cylinder	0.124	0.85	838.79	0.00137	0.3865
Spar	0.124	0.99	287.12	0.000546	0.3891

OrcaFlex Suitability

OrcaFlex is an industry standard hydrodynamic analysis software, with a range of applications such as mooring analysis, pipelay simulation and submarine sensor array deployment (Orcina, 2019). Analysis is typically performed on full-scale, validated models to determine performance against localised field data (DNV-GL, 2010). As a consequence, the applicability of *OrcaFlex* to scale models is subject to few research papers, with Paduano, Giorgi and Gomes (2020) offering the most significant investigations - Comparing *OrcaFlex*, quasi-static and experimental results, where *T* is mean tension and θ_T the tension standard deviation, the research shows an agreement between standard deviation and tension values that is further confirmed with email correspondence with Orcina (Dooley, 2020). However, further study is required to understand the implications of scale modelling, as Paduano, Giorgi and Gomes (2020) also identified areas of numerical discrepancy which are discussed in the *Discussion* section.

Theory

Numerical Statics & Dynamics

Static analysis of a mooring line concerns the system in equilibrium where force, $F = ma$, is balanced with acceleration $a = 0$ multiplied by mass m. Assuming a simplified catenary wire, the force components can be derived as the simplified free body diagram of Figure 2, or as a magnified section taken at a submerged point p on the line.

Where h is the depth from MSL to seabed, T denotes the tension for each vector of the line, D is the hydrodynamic drag force divided by the length normal to the line, F is the hydrodynamic drag force / length tangential to the line, w is the weight divided by the length of the line submerged in fluid and d is a differential with respect to the subject component.

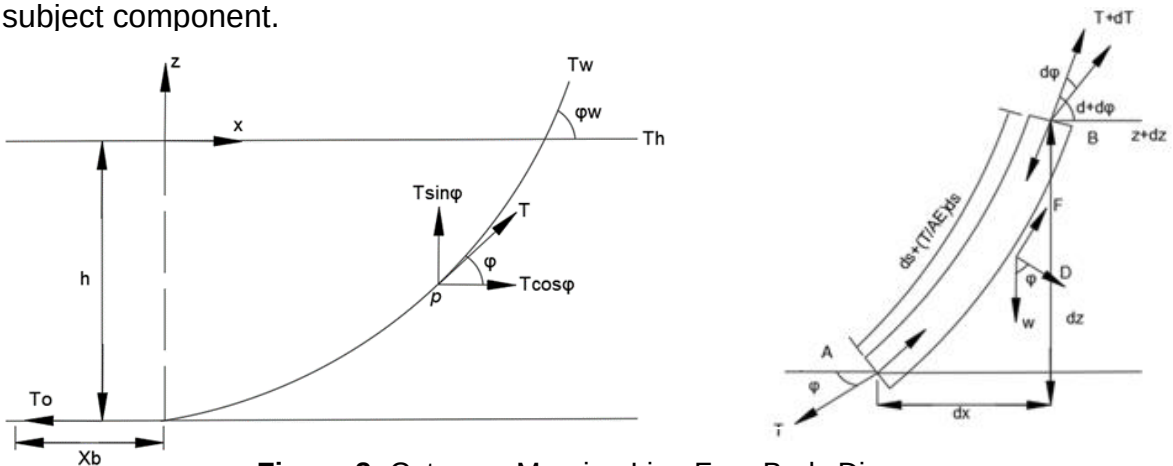

Figure 2: Catenary Mooring Line Free Body Diagram

Taking A as the lower line segment and B as the upper, the hydrostatic buoyancy can be derived as $F = -\rho g z A$ (A) or $F = -\rho g z A - \rho g A \Delta z$ (B) where A is the cross sectional area of the mooring line. The tangential and normal force components can be derived relative to their vector and line elongation $E = \frac{T}{A\epsilon}$. System static tension is hence primarily a consequence of buoyancy, weight and line hydrostatic properties such as tensile properties, axial stiffness etc.

Considering a slack line, vertical tension varies proportional to the effective weight per metre of the picked up line for $T_V(s) = W\big(s - (L - L_S)\big)$ and $T(s) = \sqrt{T_H^2 + T_V(s)^2}$. Meanwhile, for the taut lines of the OWC system, the tension is constant given that laydown length X_B is $0m$. For the modelling investigation, these derivations are the most pertinent, with others presented by Davidson & Ringwood (2017) in referenced literature.

Quantifying static line tension is relatively simple. Conversely, solutions to dynamic problems become more complex, and are typically solved using spatially discretized ordinary differential equations (ODEs) (Davidson & Ringwood, 2017) set against simplified systems. An elegant derivation, the dynamics equation is derived from Newton's Second Law, and has complexity such that solution without the use of software is arduous if not entirely unrealistic in the context of industrial application:

$$\rho_m \frac{\delta^2 r}{\delta t^2} = \frac{\delta}{\delta s}\left(\frac{T}{1+\epsilon}\frac{\delta r}{\delta s}\right) + f(1+\epsilon) \qquad [1]$$

Object Drag

Drag forces acting on a mooring line can effect low frequency (LF) device motions significantly, and presents as two main forms – Pressure drag, influencing the generation of eddies, turbulent wake and other fluid interaction effects, and viscous drag, acting as fluid interacts with a bodies surface morphology (Lie, Gao & Moan, 2007). Assuming a direct fluid approach of velocity u_o toward a submerged geometry, the fluid encounters the perpendicular projected area A_p. The resultant drag force F_K is then derived from Morison's equation:

$$F_k = \frac{(C_d \times A \times \rho \times {u_o}^2)}{2} \qquad [2]$$

Where C_d is a surface driven drag coefficient derived from the Bejan number (Be), Reynolds number (Re) and the ratio between the wet area A_W and front area A_F where $\frac{A_W}{A_F} = 1$ for a submerged shape. (Liversage, 2018) Reduction in area A, subsequently, reduces the drag force and the object's damping potential, such quantifying this behaviour in the context of submerged buoy may offer insight into whole system optimisation.

Methodology

System Setup

The Roberts & Scott (2020) 1:60 scale model was developed in *OrcaFlex* using experimental data and recorded properties, as-built during experimentation. Consequently, the system represents a full scale OWC system proposed in

WETFEET – albeit scaled – by Collins, Howey and Greaves (2018). The system is visualised in Figure 3 & Figure 4 – Note that, for Surge, Line 2 is directly connected to the actuator whereas, in Heave, the line first connects to a pulley.

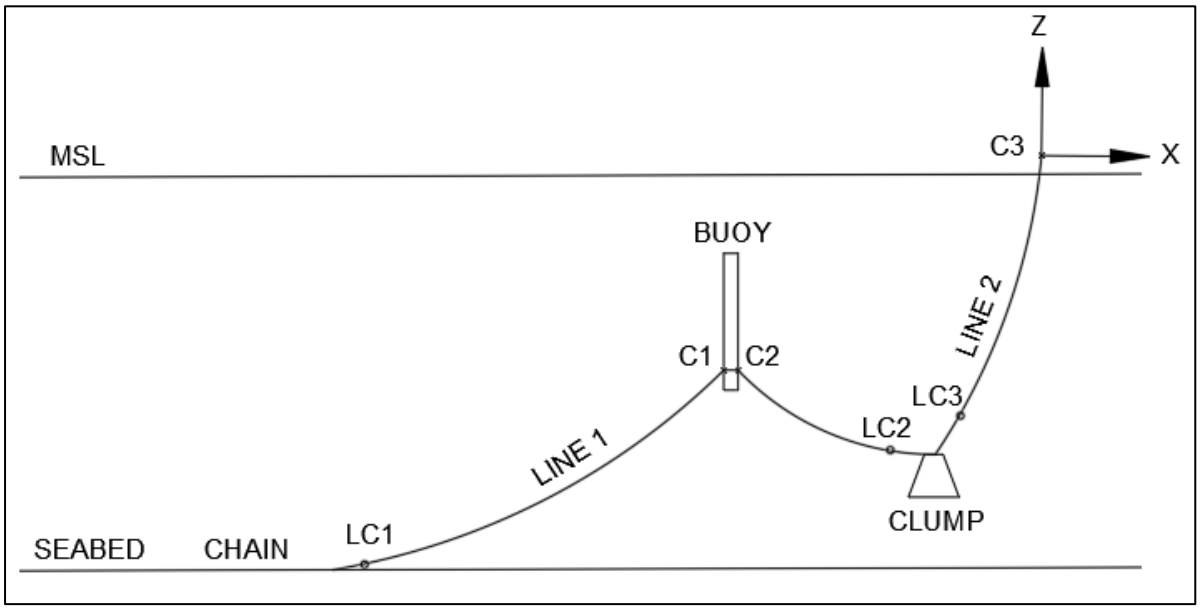

Figure 3: Heave System Setup

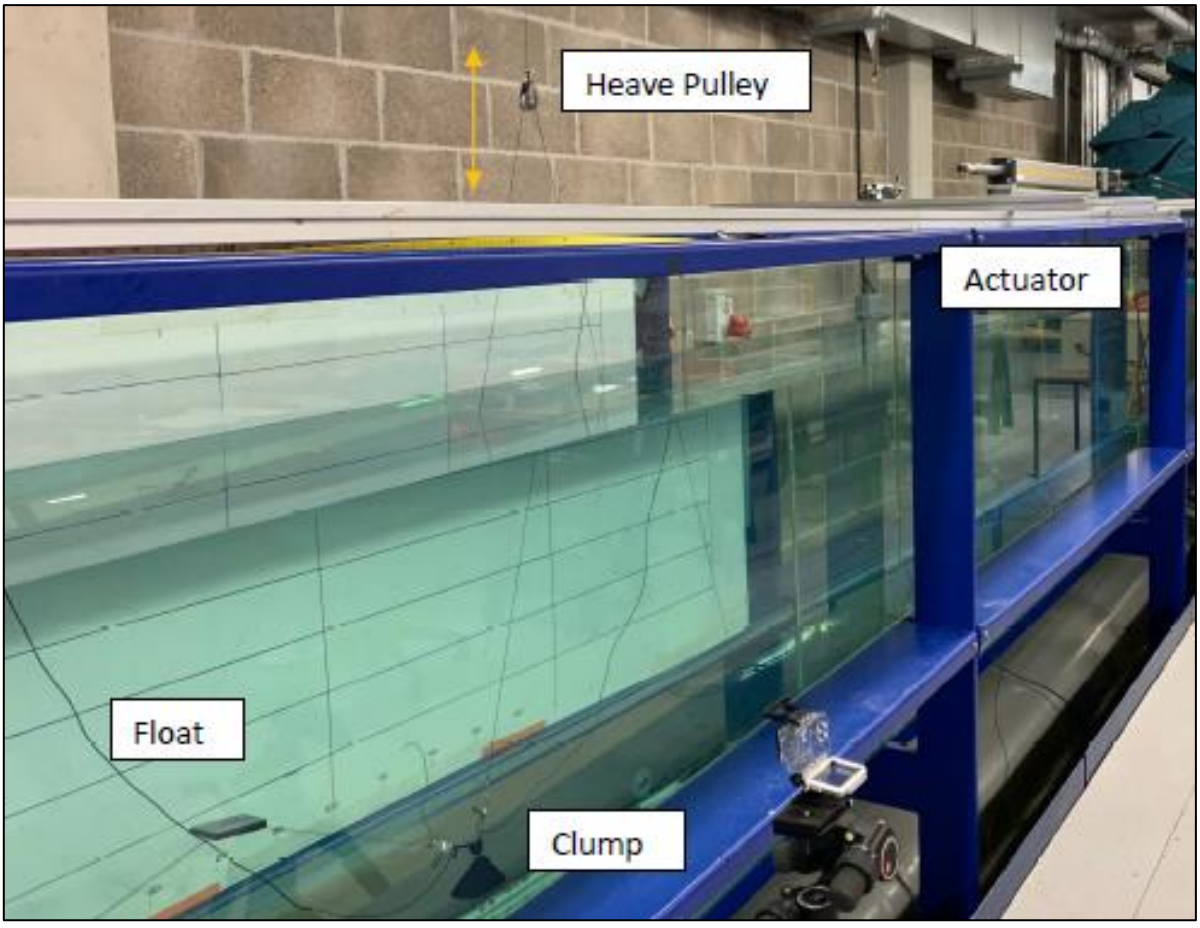

Figure 4: Heave System Physical Setup

Experimentally, the greatest discrepancies between floats were found between the Plate and Spar, due to significant aspect ratio differences. As the result, the cylindrical buoy was omitted from the numerical investigation, with justification, to reduce simulation and processing time. The buoy properties and system properties are described in the *Investigation* section, with the model is visualised in the below Figure 5.

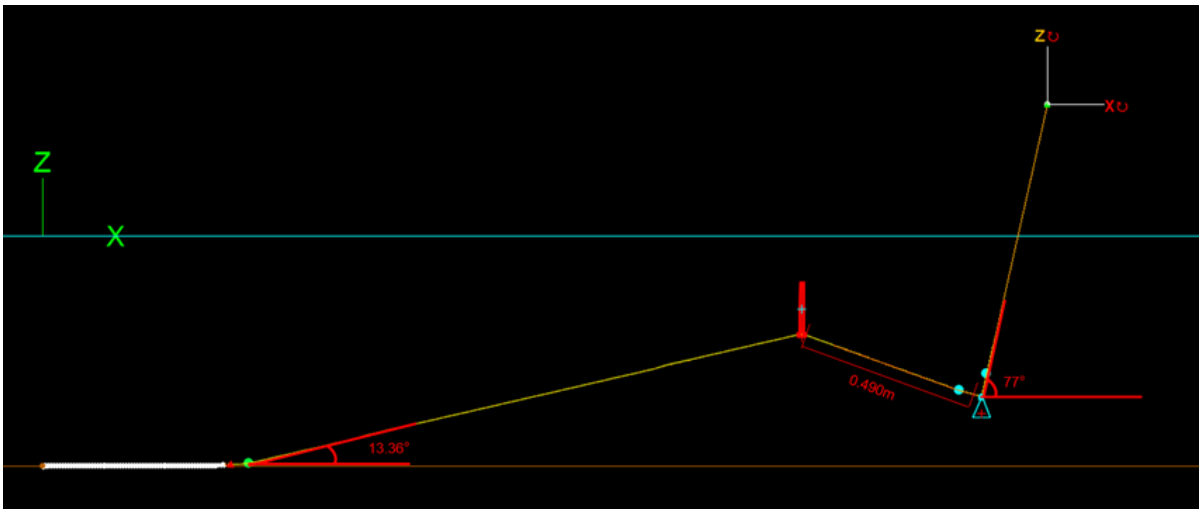

Figure 5: OrcaFlex System Setup

Environmental Load Cases

OWC excitation is simulated by actuator displacement, at a specified frequency and extension. The derived data is based on field RAO data proposed in the WETFEET study (Collins, Howey & Greaves, 2018), and summarised in Table 2 & Table 3, for a total of 36 individual load-cases.

Table 2: Heave Scaled Motion

Period (s)	Frequency (Hz)	Actuator Extension (m)
2.33	0.43	0.096
1.56	0.64	0.185
0.91	1.1	0.03

Table 3: Surge Scaled Motion

Period (s)	Frequency (Hz)	Actuator Extension (m)
2.34	0.43	0.114
1.42	0.7	0.054
0.91	1.1	0.03

Oscillation acts as an airy wave with typical sinusoidal wave characteristics and has been verified at the actuator by an *OrcaFlex* assessment of the spectral density (mm^2/hz) of motion, and by measurement of the displacement (mm) in the extension direction (Figure 6).

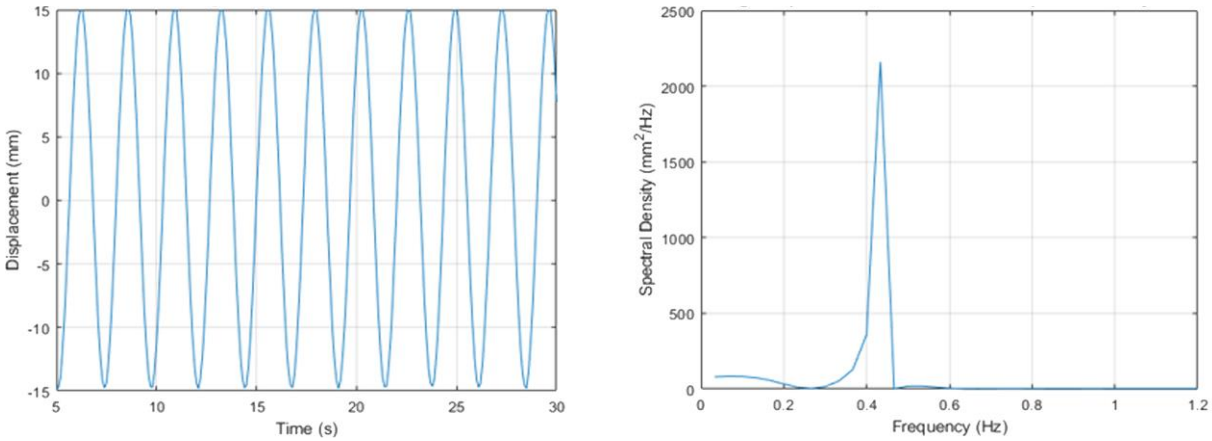

Figure 6: Displacement & Spectral Density – 0.43Hz, 30mm Surge

Lines & Connections

Chain

The *lines* of the system comprise of a laydown portion of 1mm chain, acting as the seabed anchor point, connected to 1mm dyneema acting as the primary line of the mooring system. Due to the absence of recorded hydrostatic line data, estimations were made based on the Scana Ramnas chain catalogues (Orcina, 2020), which offers scalable formula given in Table 4 used within the *OrcaFlex Line Wizard.*

Table 4: Chain Catalogue Data

Property	Formula
Outer Diameter	1.80d
Inner Diameter	0
Outer Contact Diameter	3.35d
Mass / Length	$19.9d^2$
Axial Stiffness	$0.854*10^8d^2$
Normal Drag Coefficient	2.4
Normal Drag Diameter	d
Axial Drag Coefficient	1.15
Normal Added Mass Coefficient	d/π
Axial Added Mass Coefficient	0.5

Although the properties are scalable, non-linearities are present and hydrodynamic effects may be lost, leading to discrepancies in estimated line data. A discrepancy was identified between experimental and numerical mass per unit length at 1.76N/m and 1.38Nm respectively for a 25% difference. Mass per unit length – arguably the most fundamental\ property for its influence on buoyancy and weight forces – was matched by reduction of numerical diameter d to 2.63mm. Dynamic tension was deemed to be insensitive to the change through comparison in Figure 7 and Figure 8.

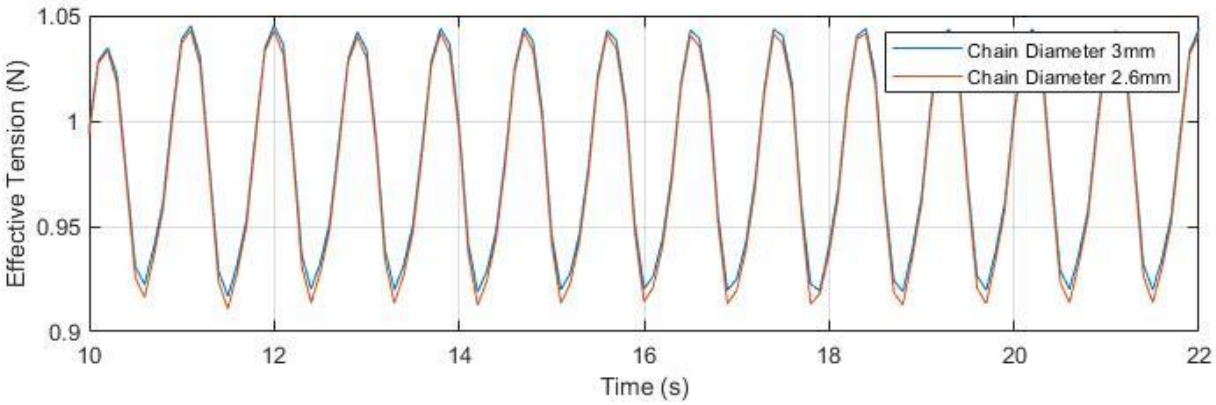

Figure 7: Surge Case 1.1Hz Ex. 114mm – Effective Tension vs. Time

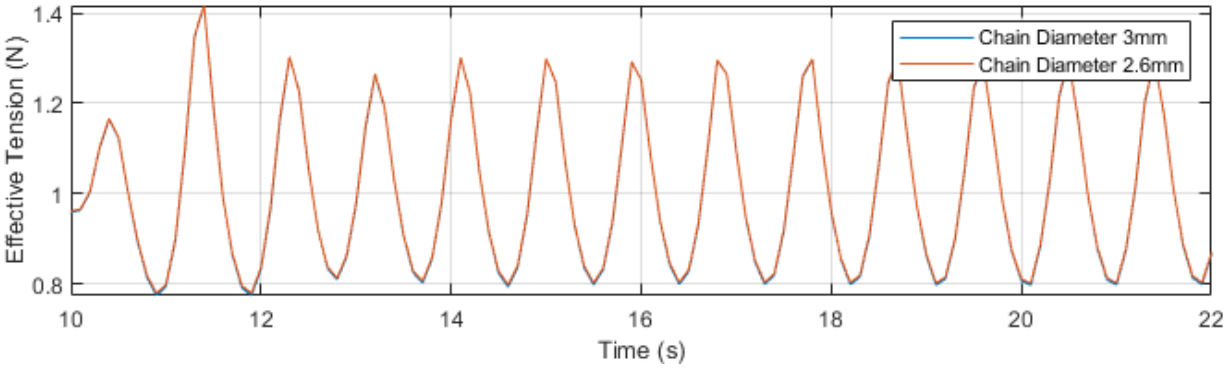

Figure 8: Heave Case 1.1Hz Ex. 185mm – Effective Tension vs. Time

Dyneema

For dyneema, the mass per unit length is derived from the specific gravity $s.g.$ of UHMWPE rope, and its material density ρ 980kg/m^3 (ProteusDS, 2019) using $s.g. = \frac{\rho_{object}}{\rho_{water}}$. Substituting the calculated density into a simple mass, density and volume equation calculates a mass per unit length value of 770E-09kg/m. The axial stiffness is then calculated by:

$$EA = \frac{100F_{\varphi}}{\varphi} \quad [3]$$

Where φ is the precent elongation at applied load F_{φ}. Percent elongation for similar UHMW Dyneema rope (SamsonRope, 2021) at 2.5mm diameter is 0.96% at 30%. Taking 30% of the minimum strength offered at this elongation – 1,400lbs, or 6228N – gives an axial stiffness of approximately 1.868KN. The variable data calculated was then applied to the *OrcaFlex* model, along with estimated *Line Wizard* data. Load cells were attached to the dyneema at line positions calculated from

experimental photographs and are given in Table 5. The chain and dyneema properties are given in Table 6 and Table 7.

Table 5: Load Cell Data

Property	Experimental	Numerical	Unit
Volume (Load Cell)	1436	N/A	mm^3
Volume (Shackle)	764.331	N/A	mm^3
Total Volume (LC + SH)	2200	2200	mm^3
Density (Fluid)	1000	1000	kg/m^3
Density (Steel)	7850	7850	kg/m^3
Mass (Shackle)	0.006	N/A	kg
Mass (Load Cell)	0.009	N/A	kg
Total Mass	0.015	0.015	kg
Weight (Total)	0.147	0.147	N
Buoyancy (Total)	0.002	0.002	N
Net Force (Total)	-0.145	-0.145	N
Drag Area X	Unspecified	89.600	mm^2
Drag Area Y	Unspecified	186.819	mm^2
Drag Area Z	Unspecified	408.667	mm^2
Drag Coefficient X	Unspecified	1.050	-
Drag Coefficient Y	Unspecified	0.820	-
Drag Coefficient Z	Unspecified	0.820	-

Table 6: Chain Properties

Property	Experimental	Numerical	Unit
Length	0.77	0.77	m
Diameter	3.00	2.63	mm
Weight per Unit Length	1.35	1.35	N/m
Mass per Unit Length	0.00	0.00	kg/mm
Axial Stiffness	Unspecified	590000	N
Drag Coeff. X	Unspecified	2.40	-
Drag Coeff Y.	Unspecified	2.40	-
Drag Coeff Z.	Unspecified	1.15	-
Nominal Drag Diameter	Unspecified	2.63	mm
Axial Drag Diameter	Unspecified	0.84	mm

Table 7: Dyneema Properties

Property	Experimental	Numerical	Unit
Length (L1)	N/A	2591.12	mm
Length (L2)	Est. 1140	1140	mm
Diameter	1	1	mm
Mass per Unit Length	Unspecified	0.0077	g/mm
Axial Stiffness	Unspecified	1.819	KN

Ultimately, the lines are subject to an estimation unique to scale modelling, due to the absence of specific catalogue data relative to chain and line type, and

discrepancy in fluid flow modelling and hydrostatics may be present as a consequence of non-linearities.

Clump, Spar & Plate

The clump weight and buoys have been modelled as a 6D lumped buoy, where the hydrostatic values act upon the centre of mass and volume through three translational and three rotational degrees of freedom (Orcina, 2020). The clump and spar geometries are visualised in Figure 9.

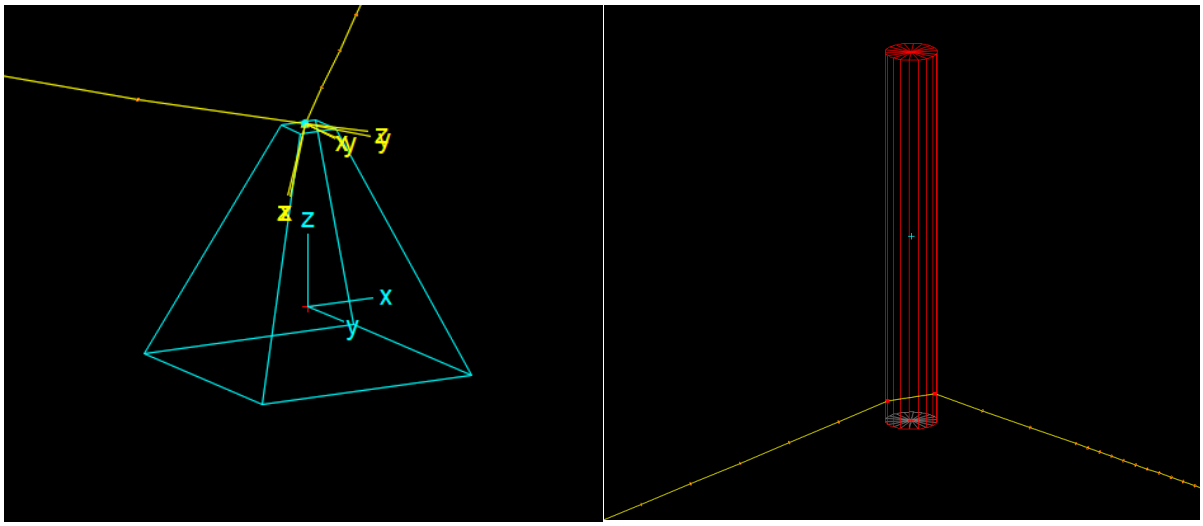

Figure 9: OrcaFlex Clump & Spar Visualisation

While the spar and plate buoys have hydrostatic data calculated by *OrcaFlex* measurement of geometry, the *lumped* clump weight relies on calculated input data and estimation. The weight f_w and buoyancy f_b forces of the clump weight are calculated as a function of mass and volume (Orcina, 2020):

$$f_w = -mgu_z \;\&\; f_b = \rho g V_{wet} u_z \qquad [4, 5]$$

While the method for calculating drag force f_{D_n} and drag moment M_{Rn} are derived from Morison's equation described in the *Object Drag* section, with input components x_n varied where n is the global coordinate direction:

$$f_{Dn} = -p_w \left(\frac{1}{2}\right) \rho C_{Dn} A_n v_n |v| \;\&\; M_{Rn} = -\frac{1}{2} p \rho C_{Dn}^r A M_n \omega_n |\omega| \qquad [6, 7]$$

The drag force and moment will vary in practice with body acceleration influencing velocity v, or with variance of perpendicular drag area A_n or moment AM_n. As area A is assuming a quadrilateral drag area, the actual drag force of a complex body such as the clump weight or load cell is approximated. Similarly, volume has been estimated, and so both the buoyancy and drag properties are subject to error when compared with the experimental model. The formula is visualised relative to the global axis in Figure 10 and Figure 11.

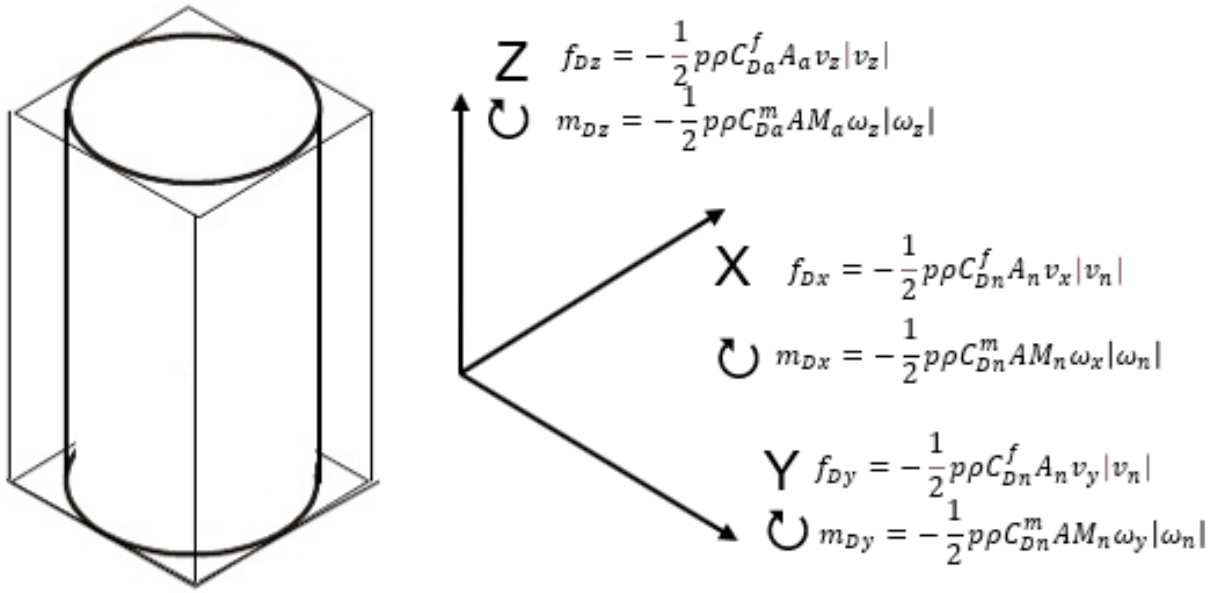

Figure 10: Cylindrical Drag Force Diagram

The properties of the Clump, Spar and Plate are given in Table 8, Table 9 and Table 10, where the drag moment of area can be calculated as $d^5/60$ and $d^4/32$ for a circular disk of diameter d (Orcina, 2020) and a cylindrical surface respectively.

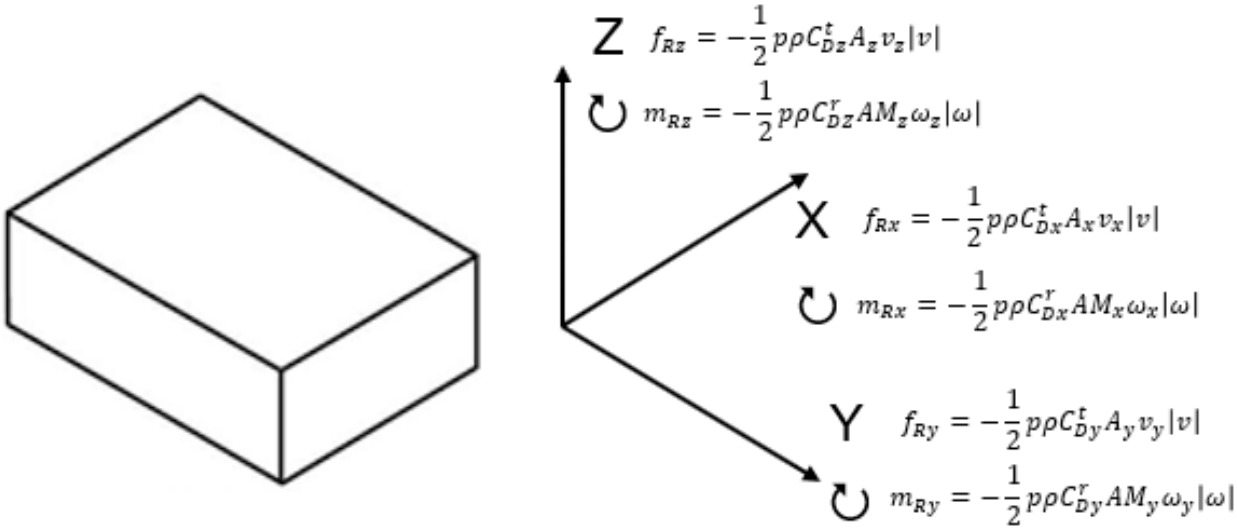

Figure 11: Plate Drag Force Diagram

Table 8: Cylinder Properties

Property	Experimental	Numerical	Unit
Weight	0.503	0.503	kg
Density (Lead)	11342	11342	kg/m^3
Volume	0.0000473	0.0000473	m^3
Drag Area X	Unspecified	787	m^2
Drag Area Y	Unspecified	3727	m^2
Drag Area Z	Unspecified	12691.17	m^2
Drag Coeff. X	Unspecified	0.82	-
Drag Coeff. Y	Unspecified	1.14	-
Drag Coeff. Z	Unspecified	0.82	-
Mass Moment of Inertia X	Unspecified	1.17	$g*mm^2$
Mass Moment of Inertia Y	Unspecified	1.17	$g*mm^2$
Mass Moment of Inertia Z	Unspecified	1.17	$g*mm^2$
Drag Mo. Area X	Unspecified	19.31	mm^2
Drag Mo. Area Y	Unspecified	19.31	mm^2
Drag Mo. Area Z	Unspecified	19.31	mm^2
Rotational Drag Coeff. X	Unspecified	0.82	-
Rotational Drag Coeff. Y	Unspecified	1.14	-
Rotational Drag Coeff. Z	Unspecified	0.82	-

Table 9: Spar Properties

Property	Experimental	Numerical	Unit
Density	41	41	kg/m^3
Volume	55200	41000	mm^3
Mass	0.0022632	0.00162	mm
Buoyancy Force	0.3891	0.38672	N
Surface Area	287.12	287.121	mm^2
Radius	9.56	9.56	mm
Diameter	19.12	19.12	mm
Length	192.37	143	mm
l/d Ratio	10.06255	7.4791	-
Drag Area Normal	Unspecified	3880	mm^2
Drag Area Axial	Unspecified	0.000287	mm^2
Drag Coeff Axial	0.99	0.99	-
Drag Coeff Normal	Unspecified	0.82	-
Drag Force Axial	0.000546	0.002185316	N
Mass Moment of Inertia X	Unspecified	7.03536	kg/m^2
Mass Moment of Inertia Y	Unspecified	7.03536	kg/m^2
Mass Moment of Inertia Z	Unspecified	0.140348	kg/m^2
Axial Drag Moment	Unspecified	42588.09256	mm^5
Normal Drag Moment	Unspecified	0.427	mm^5

Table 10: Plate Properties

Property	Experimental	Numerical	Unit
Density	41	41	kg/m³
Volume	55200	60000	mm³
Mass	0.0022632	0.0022632	kg
Buoyancy Force	0.3817	0.382	N
Surface Area	5521.9761	5521.9761	mm²
Width	74.31	74.31	mm
Length	74.31	74.31	mm
Thickness	10	10	mm
Drag Area Normal	0.0007431	0.0007431	mm²
Drag Area Axial	5521.9761	5521.9761	mm²
Drag Coeff Axial	1.28	1.28	-
Drag Coeff Normal	Unspecified	1.16	-
Drag Force Axial	0.054339779	0.054339778	N
Mass Moment of Inertia X	Unspecified	1.06	kg/m²
Mass Moment of Inertia Y	Unspecified	1.06	kg/m²
Mass Moment of Inertia Z	Unspecified	2.083	kg/m²
Axial Drag Moment	Unspecified	69813765.29	mm⁵
Normal Drag Moment	Unspecified	23200	mm⁵

Buoyancy has been matched against Roberts (2020) data by specifying a volume V_{wet} in the buoyancy equation $f_b = \rho g V_{wet} u_z$.

Property Checklist

The above investigation section focuses on aspects that may have influenced system dynamics. Further, system properties have been given in Table 11, which are less significant. From evaluation, the two principal drivers of dynamic discrepancies are the defined point of the actuator connection, and the mass properties of the clump weight.

Results

Static Line Force

The static line force (SLF) equilibrium was measured by Scott (2020) at each load cell, for the surge and heave rigging, and forms the basis for comparison against the *OrcaFlex* SLF in Table 12.

Table 11: Validation Checklist

Property	Validated	Information
Additional Line for Load Cell (3)	✔	Digitization + Length Check
Buoy – Cylinder Buoy	✔	Geometric + Calculation
Buoy – Plate	✔	Geometric + Calculation
Buoy – Spar Buoy	✔	Geometric + Calculation
Chain Anchor Point	✔	Geometric
Chain Diameter	✔	Mass p/unit Length + *d* sensitivity
Chain Length	✔	Given
Connection Point (L1) Cylinder	✔	400mm from AutoCad Digitisation
Connection Point (L1) Plate	✔	380mm from AutoCad Digitisation
Connection Point (L1) Spar	✔	AutoCad Digitisation + Estimation
Connection Point of Line Clump	✔	AutoCad Digitisation
Constraint / Actuator Position	~	Estimated
Dyneema Properties	✔	Axial Stiffness, Mass p/unit Length
Full System Statics	✔	Verified by Given Angle Checks
Line 1 Length	✔	Given
Line 2 Length	✔	AutoCad Digitisation, Estimation
Line Azimuths, Declinations etc.	✔	Advised + Verified at Orcina
Load Cell Position (1)	✔	AutoCad Digitisation
Load Cell Position (2)	✔	AutoCad Digitisation
Load Cell Position (3)	✔	AutoCad Digitisation
Position of Clump Weight	✔	Equilibrium of Angles / Constraint
Properties of Clump Weight	~	Estimated

Table 12: Static Line Force Values (Newtons)

Load Cell	Plate Experimental	Plate OrcaFlex	Spar Experimental	Spar OrcaFlex
1	0.942	0.894	0.935	0.904
2	2.040	0.902	2.095	0.914
3	3.810	4.460	3.620	4.447

Evaluation of the SLF indicates an inconsistency between both the gradient of tension increase between LC1 and LC2, and the maximum static line force observed. SLF tension appears distributed throughout the system in the experimental results, whereas tension is concentrated at Line 2 LC3 in the numerical model. Comparison of the tension gradients are given in Figure 12 and show constant tension across the *OrcaFlex* line 1 and a concentration of tension at the clump weight, while the experimental data exhibits a gradient of approximately 44% and 46% between LC1 and LC2, indicative of the taut line effect on restricting tension distribution.

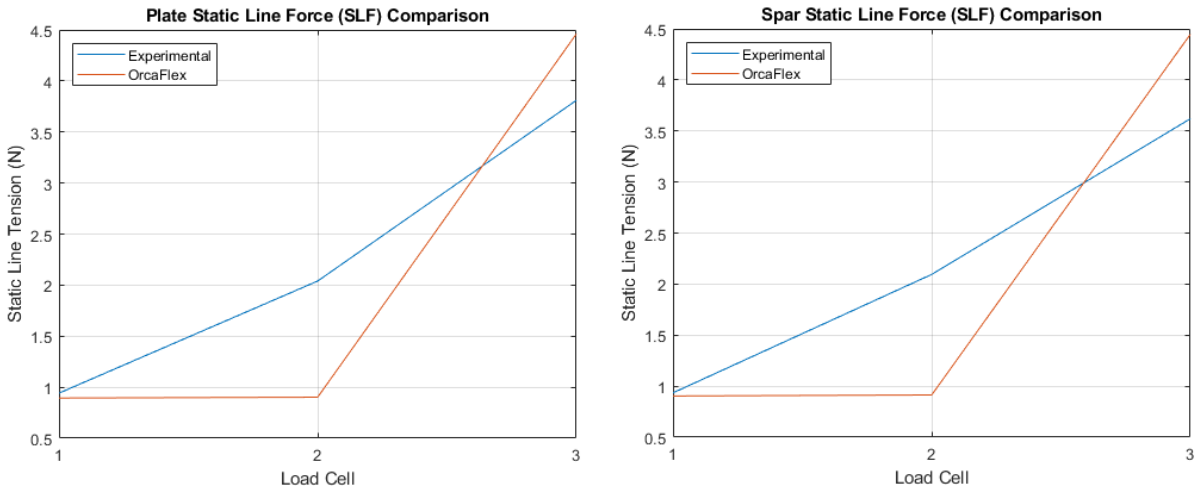

Figure 12: Static Line Force (SLF) Comparisons

Dynamics

Maximum Mean Effective Tension

The Maximum Mean Effective (MME) tensions were derived as an average of effective tension peaks between the time period of 0 – 30 seconds. Quantifying the MME tension allows for a direct comparison to the experimental results without extreme tension values skewing the data. An example of peak evaluation in MATLAB is plotted in Figure 13.

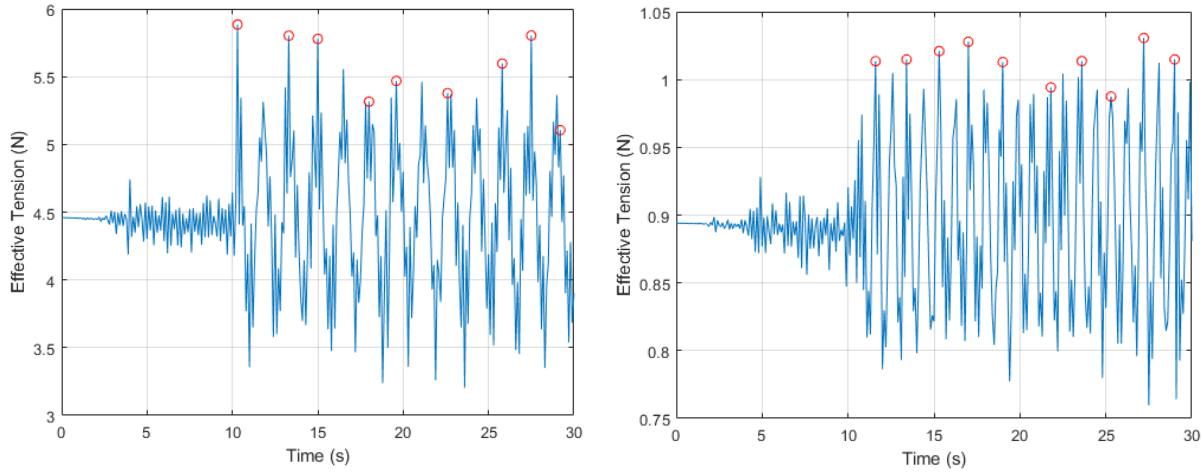

Figure 13: MATLAB Specified Peak Tension Example

To avoid repetition of numerical observations, the general trends exhibited in the MME tension plots have been described below. Each plot is compiled to allow for comparison of the *OrcaFlex* and experimental data. The general trends are as follows, evaluated by the *OrcaFlex* data:

- The MME tension is significantly greater at LC3 and increases with oscillation frequency and extension which conforms to the experimental findings. However, the actual tension exhibited varies, for a mean percentage of difference of 11% for Heave Spar, 11% for Heave Plate, 6% for Surge Spar and 12% for Surge Plate.

- Tension is maintained between LC1 and LC2, which is contrary to the positive tension gradient exhibited along the connected line in the experimental data. This is likely an effect of taut line tension.

- The effect of drag area variance in terms of trend typically follows the identified behaviour found in the experimental data or is inconclusive. For example, a Spar buoy exhibits higher tension at LC3 during Heave motion at a frequency of 1.1Hz and an extension of 185mm.

- The spar and plate buoys show little MME tension difference between floats when the OWC is acting in the Surge degree of motion. Heave, conversely, shows a better representation of experimental trends with the plate exhibiting higher tensions in 0.43Hz and 0.64Hz at 185mm extension, while the spar exhibits higher tensions at a frequency of 1.1Hz, extension 114mm.

- Surge numerical values for both geometries are near equivalent, while a degree of difference is present in the experimental data, although understated compared to Heave. Heave, conversely, shows a reasonable fit between the data with the plate exhibiting higher tension in Heave 0.64Hz and 0.43Hz 185mm extension, and the spar higher in 1.1Hz 114mm. Otherwise, the data is inconclusive.

Table 13: Mean Percentage Differences

Case	LC1	LC2	LC3
Heave Spar	11.05%	14.54%	10.29%
Heave Plate	8.04%	17.01%	8.38%
Surge Spar	5.38%	4.48%	8.39%
Surge Plate	13.70%	12.48%	11.42%

The compiled MME tension graphs (Figure 14) have been provided below, plotted against the key specified in Table 14, with a brief description of evaluated tensions using the *OrcaFlex* model as a foundation.

- Heave 0.43Hz: OrcaFlex specific – Plate and Spar show very little difference in effective tension and can be considered inconclusive. Line tensions are higher at LC3 compared to the experimental results, and lower at LC1 and LC2.

- Heave 0.64Hz: The plate features higher tensions in both experimental and OrcaFlex data, compared to the Spar, although the spar features higher tensions at LC3. Resonance behaviour is not immediately apparent in the 185mm resonance case.

- Heave 1.1Hz: Trends equivalent between experimental and Orcaflex, with spar at greater tension at LC1 and LC2 aside from 114mm case.

- Surge 0.43Hz: OrcaFlex spar and plate values show little difference and are inconclusive. Difference between values at LC3 is significant, with the experimental tension lower with a greater difference between each geometry.

- Surge 0.64Hz: Inconclusive results between OrcaFlex geometries as little difference. Differences significant for LC1 and LC2 114mm between OrcaFlex and experimental, although the magnitude of difference agrees.

- Surge 1.1Hz: Little difference, greatest difference at LC1 and LC2 144mm as in Surge 0.64Hz. Inconclusive results between OrcaFlex shapes, greater magnitude of difference between experimental geometries.

For clarity, numerical data has been omitted from the plots. The results are presented in comparative plots according to the key given in Table 14 where solid lines represent the *OrcaFlex* data.

Table 14: Line Key

Case	Line Colour	Data Source	Geometry
- / - -	RED	OrcaFlex / Experimental	Plate
- / - -	BLUE	OrcaFlex / Experimental	Spar

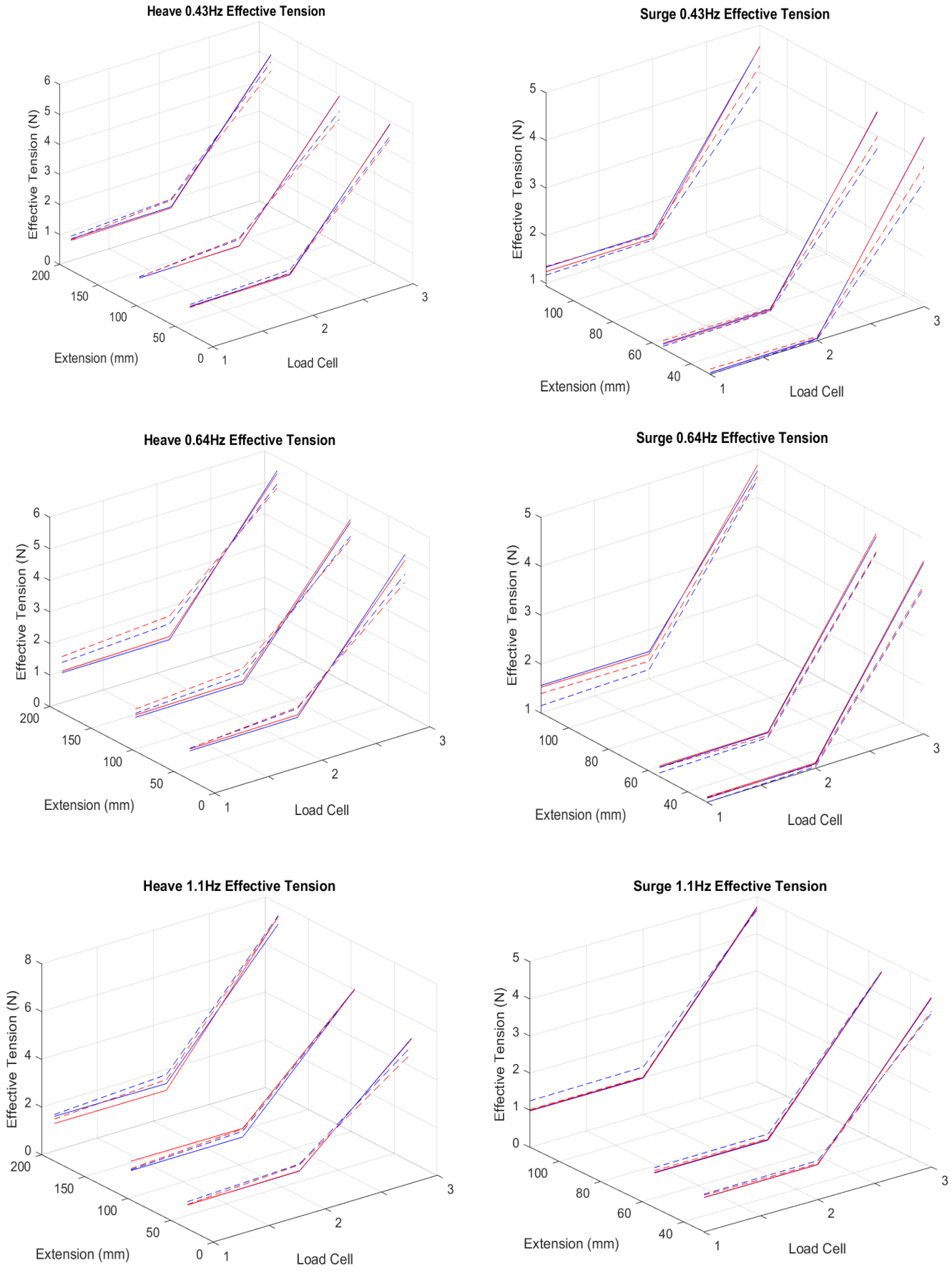

Figure 14: Compilation of Maximum Mean Effective Tensions (See Table 14 Key)

Driving Frequency Amplitude

Six driving frequency amplitude plots were evaluated to determine the effect of aspect ratio variance. Driving frequency is defined as tension loaded at the oscillation frequency based on a Fast Fourier Transform (FFT) (Bingham *et al.*, 2015) and gives an indication as to what motion is being distributed through the system relative to the signal produced by the OWC motion. It is also a method used by George Roberts (2020) which allows for comparison of frequency trends.

Evaluation of the driving frequency shows that, apart from LC3 readings during Heave motion at 1.1Hz, 114mm extension, the driving frequency of the spar across all load cells is greater than the plate buoy. This same behaviour was exhibited in the experimental model and presents the relation of increased DFA because of reduced surface area.

The driving frequency amplitude graphs have been plotted (Figure 15), as before with discussion of each frequency and motion case below:

- Heave 0.43Hz: The plate features the lowest DFA values in driving frequency or were inconclusive. The same behaviour was exhibited in the experimental results.

- Heave 0.64Hz: The greatest difference between DFA in all frequencies is exhibited here and was originally detected in the experimental results. However, extension at 34mm proved inconclusive.

- Heave 1.1Hz: Differences are present when compared to the experimental data, particularly at Load Cell 3 of 114mm and 185mm. However, the mooring system is uncontrolled >34mm (Roberts, 2020), and so the results may suffer from discrepancies

- Surge 0.43Hz: The plate features lower DFA values compared to the spar at higher extensions or data is inconclusive. Both the experimental and numerical data suggest a loss of DFA between load cell 2 and 3, with the plate exhibiting a loss in DFA which was not present in the experimental data.

- Surge 0.64Hz: The plate experiences a loss in DFA between LC2 and LC3 not present experimentally. However, the plate features significantly lower DFA values compared to the spar, equivalent to the experimental data, with a similar gradient.

- Surge 1.1Hz: The spar features lower DFA values in both the experimental and numerical model, although at the lower extensions are inconclusive in the numerical model. Spar features slightly higher DFA at LC3 than the plate which is not present in the experimental data.

- For clarity, numerical data has been omitted from the plots as before. The colour key is as given in Table 14.

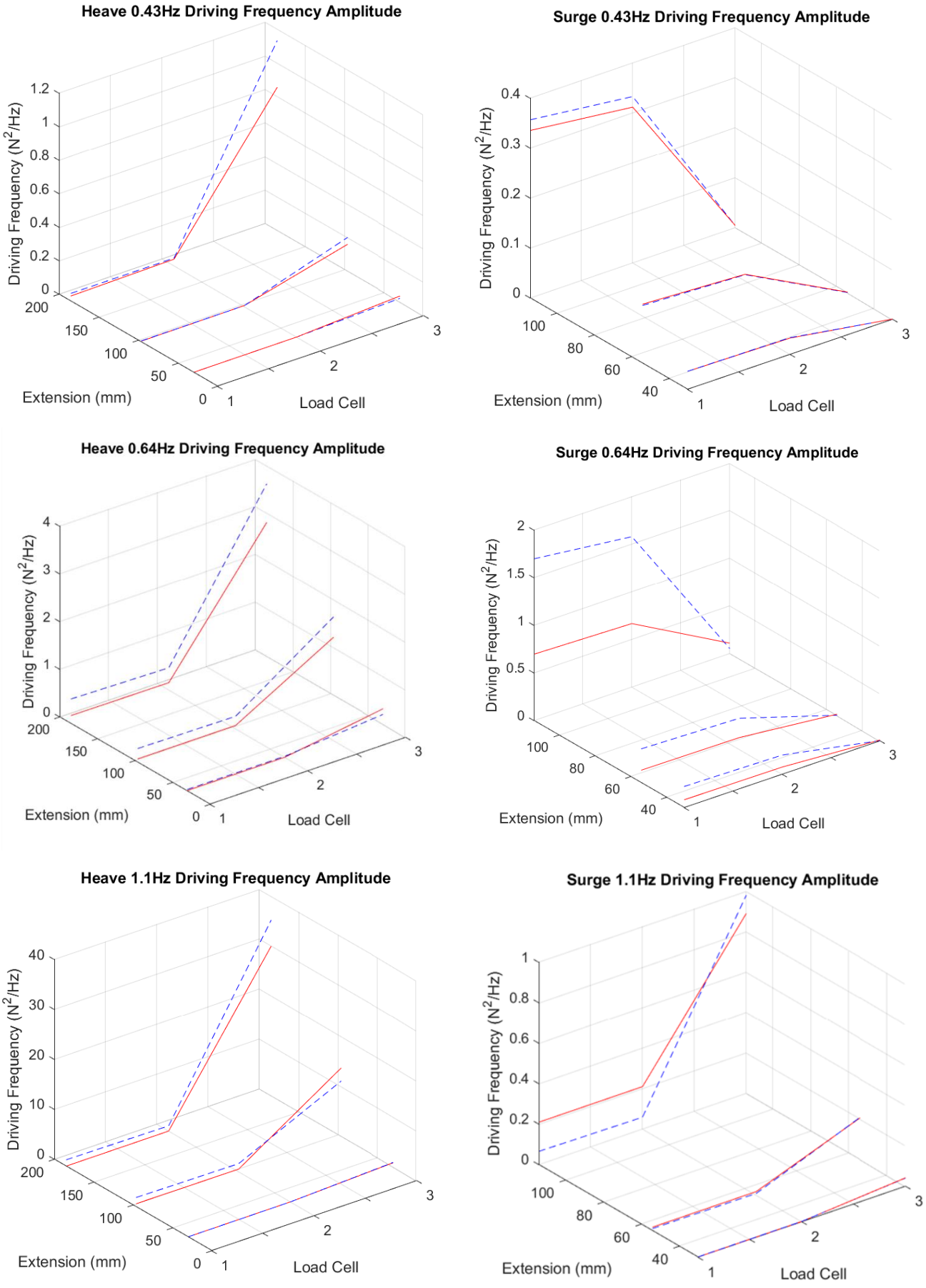

Figure 15: Driving Frequency Amplitude Graphs (See Table 14 Key)

Plate Experiment

To investigate further the impact of float surface area on driving frequency and to further validate the model's ability to predict behaviour, a plate of drag area 30% greater than the original was proposed, for an increase in perpendicular drag area of 5521mm² to 7177mm²**.** Taking the case Heave 0.64Hz Flat Plate, 96mm extension – where oscillation is significant enough for drag area to have a driving impact, and prior to uncontrolled system motion causing lagged movement – Roberts (2020) proposes that the model should exhibit less driving frequency with an increase in drag area. The results have been divided by Load Cell and are given in Figure 16, Figure 17 and Figure 18 for LC1, LC2 and LC3.

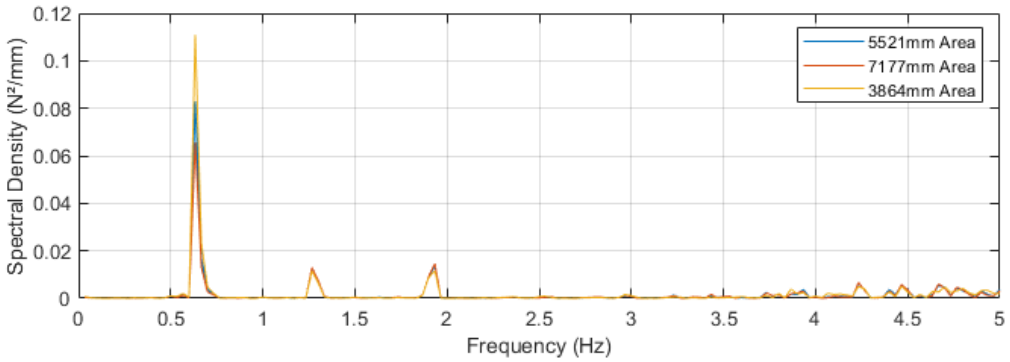

Figure 16: Heave Area Increase LC1

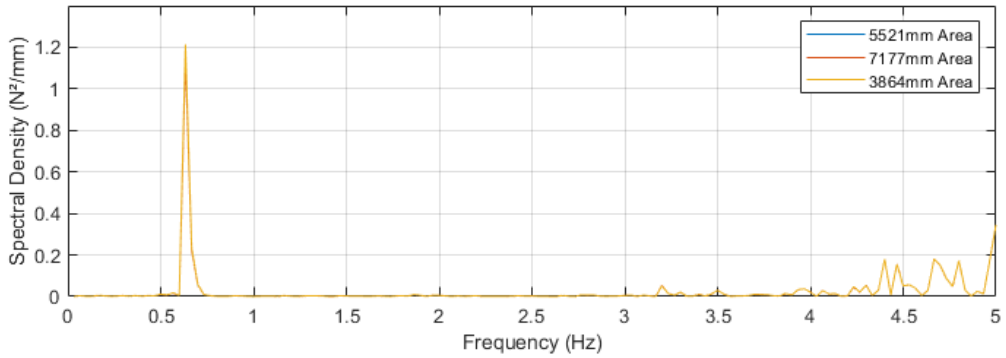

Figure 17: Heave Area Increase LC2

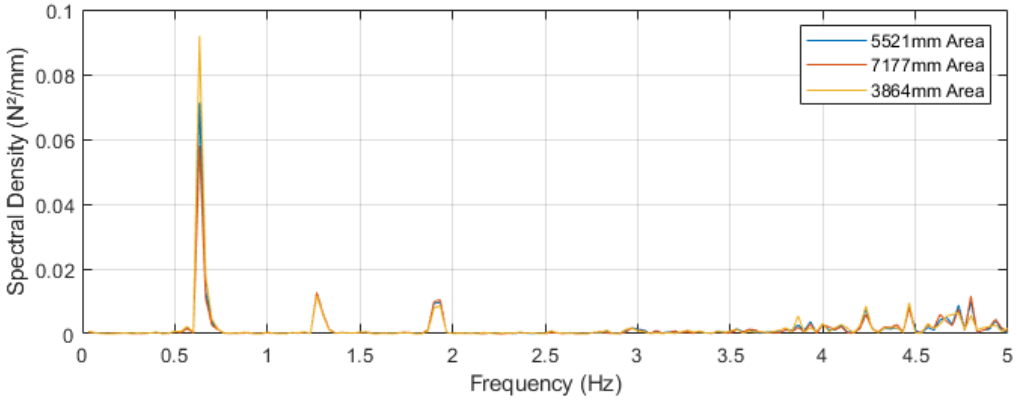

Figure 18: Heave Area Increase LC3

Evaluation based on the above graphs shows a decrease in DFA with increased frontal area at the system frequency, echoing the findings of Roberts (2020) for a

case where buoy displacement is maximum. It is recommended for additional study to be performed to quantify the effects further.

Discussion

Data Analysis

SLF Tension
The static line forces (SLF) in Surge and Heave present differently in the experimental and numerical data. As the SLF quantifies equilibrium tensions, it is necessary to understand what factors influenced the differences, as offset tensions in equilibrium can skew the dynamic tensions which tend to act around the mean SLF, as seen in Figure 19.

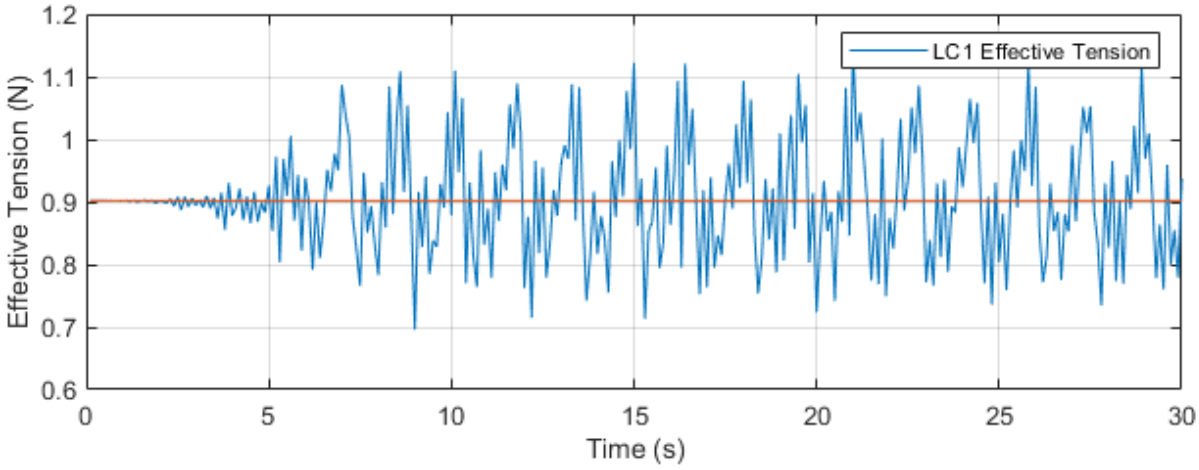

Figure 19: Tension Acting Around SLF – Heave 0.64Hz Plate

First, discrepancy between specified clump mass influenced the line mechanics significantly. Two clump masses were proposed in the experimental data – 0.598kg by Roberts, and 0.509kg by Scott. While implementation of the mass at 0.509kg lowered the SLF favourably, from a tension mean of 5.7N to 4.5N, the discrepancy introduced an element of potential hydrostatic difference in the system.

Fundamentally, the mass of a submerged body influences it's weight force $f_w = -mgu_z$, which counteracts the volumetric buoyancy force $f_b = \rho g V_{wet} u_z$. The clump weight and line connections can be simplified into the free body diagram in Figure 18 where φ_1 and φ_2 represent the angle to Z for Line 1 and Line 2, and with T_1 and T_2 denoting the tension.

As weight force w magnitude increases, angle φ_2 reduces until the tension T_2 reaches the line minimum breaking load or the seabed is reached. Solving the mechanics of the system with each clump mass, based on Figure 18 model angles, SLF tension T_2 differs by 17% for 3.921N and 4.412N. With the dynamic tension tendency to act around the SLF, it is evident that discrepancy between recorded experimental data may have influenced dynamics considerably. Note too that Scott's static line forces are in some instances higher than Roberts (2020) *dynamic* line

forces, which is illogical given the finding that MME tension acts around the SLF, casting a degree of doubt over the evaluation.

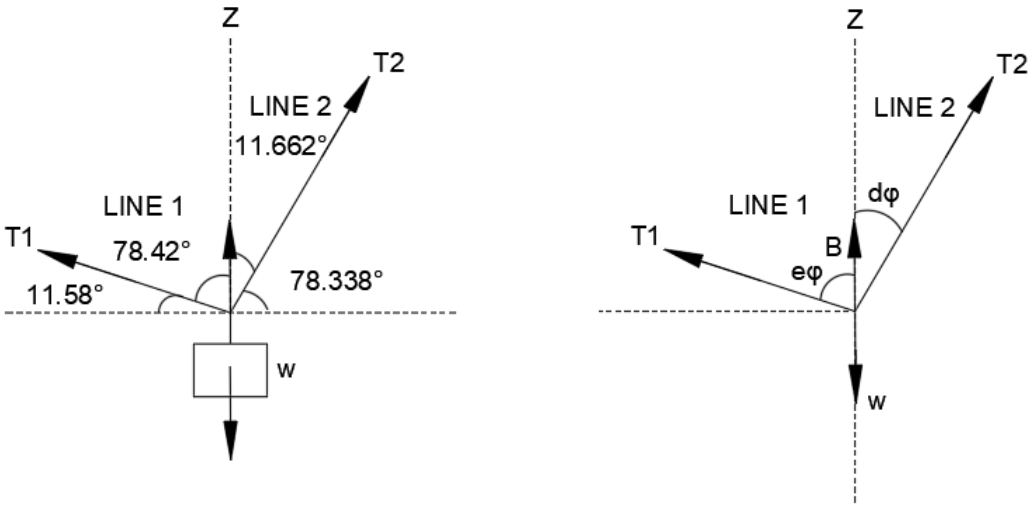

Figure 20: Line Mechanics Free Body Diagram

Taut Line Modelling

Evaluation of SLF tension and MME tension finds that tension is modelled as near constant between Load Cell 1 and Load Cell 2, which are attached to a single line portion in *OrcaFlex*. Taut line tension T is constant at any point on the line, and variance in angle θ_w is insignificant to line tension. It is theorized that the lack of tension gradient between Load Cell 1 and Load Cell 2 regards taut line tension – Taking the earlier mechanics problem of Figure 18 and introducing physical float buoyancy T_B, the actual tension acting on Line 1 load cell 2 will be $T_1 + T_B$. Meanwhile, at the anchor point Load Cell 1, the tension is a consequence principally of buoyancy force T_B, given the chain is resting on the seabed with laydown length X_B. Visualised in the free body diagram of Figure 21, the tension of Line 3 is found by solving the mechanics problem of Figure 20. Similarly, the tension of Line 2 is found through the mechanics problem *and* the tension added due to float buoyancy. Finally, the tension of Line 1 is influenced by the buoyancy *only.*

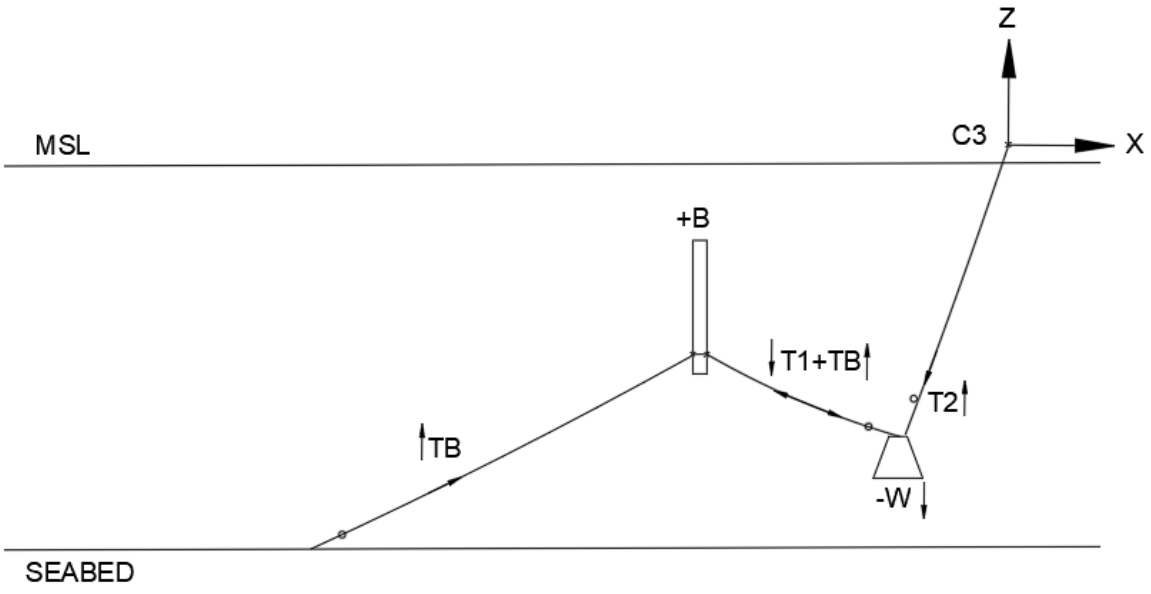

Figure 21: Tension Diagram

Although this is simplified, omitting line buoyancy, axial stiffness and other properties, it is clear a gradient of tension should be modelled between LC1, LC2 and LC3 as a result of these forces, which is not evident in OrcaFlex. It is theorized that, based on the tension methodology outlined by Orcina (2020) that line end nodes receive tension calculation *first* and the discretized mid-line nodes receive two tension forces from the line segments either side. Simply, each line segment models the tension as calculated at either end node which is identified as continuously taut such that $T_{N1} = T_{N2}$, and the added tension from the float buoyancy is omitted.

Standard Deviation

The stiffness of the system is evident in evaluation of the standard deviation of MME tension (Smith, 2011), which was discovered to act around the SLF value found in the *SLF Tension* discussion. Considering a flat plate moving in Heave, the standard deviation of effective tension was extracted from the experimental and OrcaFlex data and plotted in Figure 23, Figure 24, and Figure 25. A visualised example is given in Figure 22 for LC1, extracted from OrcaFlex, with a standard deviation σ of 0.056N. Load Case ID numbers are allocated according to Table 15.

Table 15 Load Case ID

Case ID	Frequency / Extension
1	0.43Hz 30mm
2	0.43Hz 96mm
3	0.43Hz 185mm
4	0.64Hz 30mm
5	0.64Hz 96mm
6	0.64Hz 185mm
7	1.1Hz 30mm
8	1.1Hz 96mm
9	1.1Hz 185mm

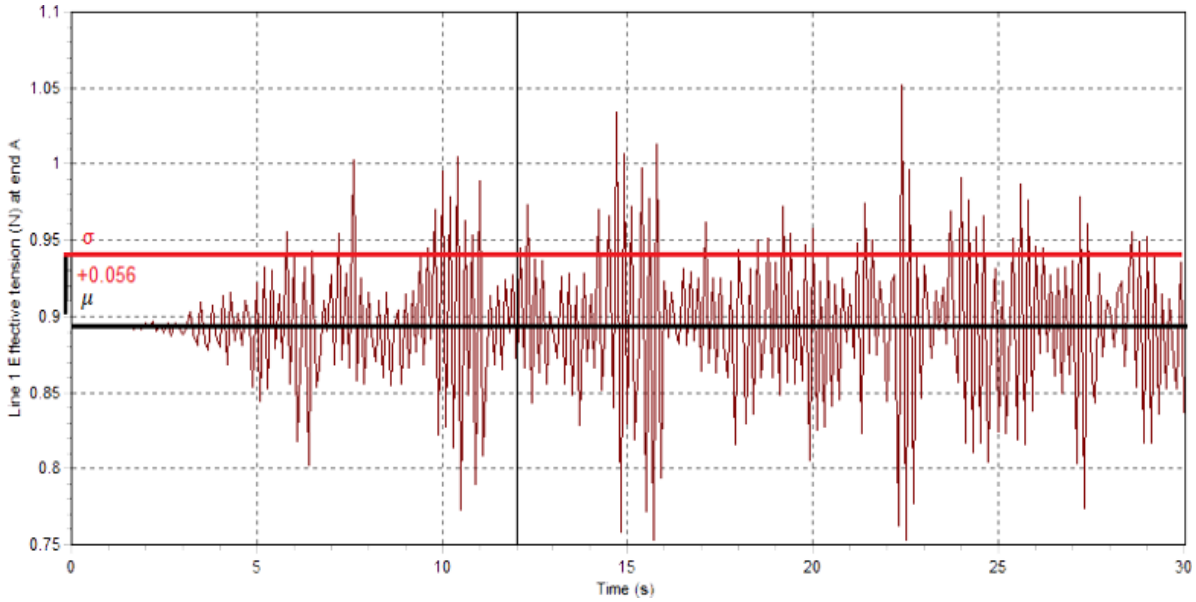

Figure 22: Standard Deviation of LC1 in Heave (0.42Hz Flat Plate 30mm)

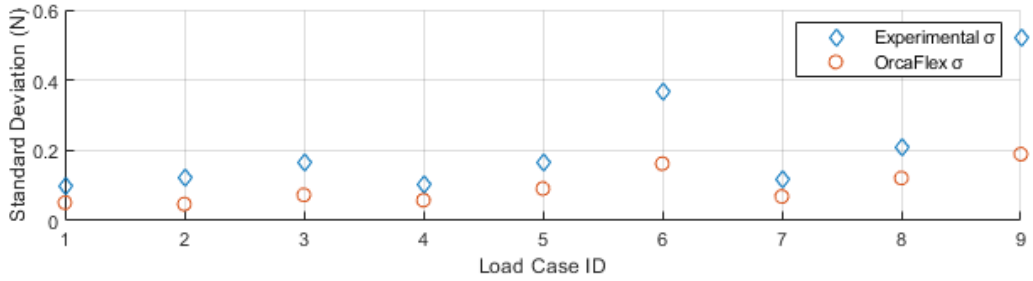

Figure 23: Standard Deviation LC1

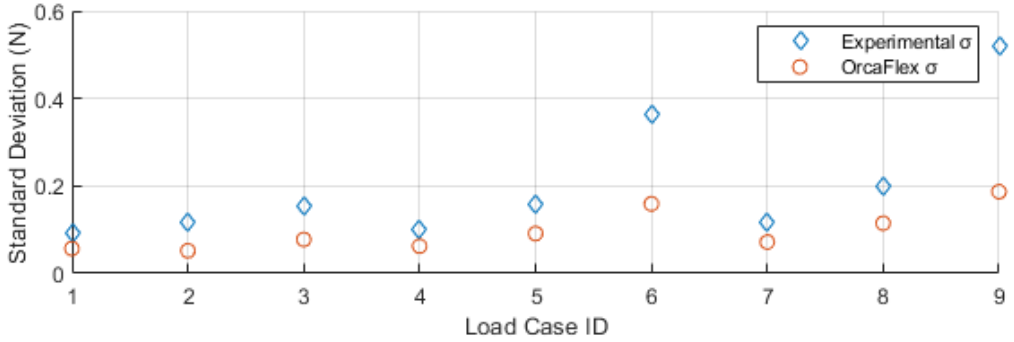

Figure 24: Standard Deviation LC2

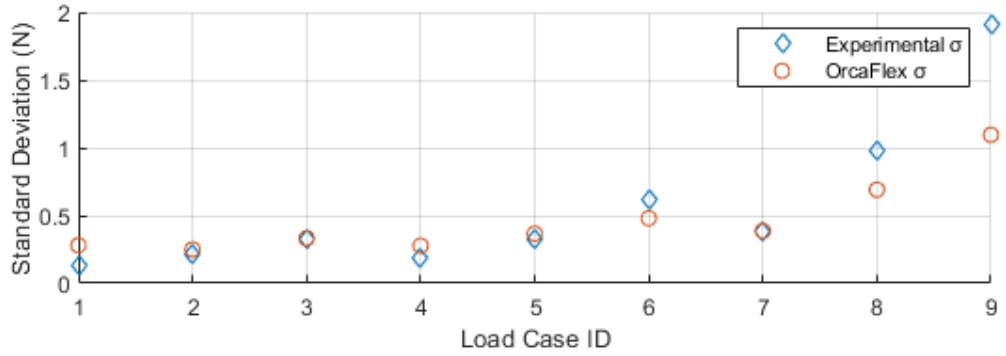

Figure 25: Standard Deviation LC3

A higher standard deviation indicates a wider range of tension from the SLF, where 68.27% of the effective tension values lie. This may be represented mathematically by the following equation, where μ is the mean of distribution:

$$(1)\ \Pr(\mu - 1\sigma \leq X =< \mu + 1\sigma) \approx 68.27\% \quad [8]$$

$$(2)\ \Pr(\mu - 2\sigma \leq X =< \mu + 2\sigma) \approx 95.45\% \quad [9]$$

$$(3)\ \Pr(\mu - 3\sigma \leq X =< \mu + 3\sigma) \approx 95.45\% \quad [10]$$

Based on equation (1), the experimental results feature a significantly wider range of effective tension distribution encapsulating 68% of values at LC1 and LC2. However, at LC3, matched standard deviation values indicate an equivalent range of tension, although Load Case 8 / 9 are not a reasonable representation due to *OrcaFlex* dynamic failure <30s. An artificial element of stiffness appears introduced into the system by the taut *Line 1*, likely a consequence of taut modelling as described in the section *Taut Line Modelling,* thus limiting the accuracy of tension measurement

which will contribute MME tension numerical discrepancies. A wider range of standard deviation may also indicate a greater magnitude of float displacement, or experimental chain lift-off that promotes a repetitive snap loading effect (Touzon, 2020). However, this requires further investigation.

Velocity Influence

The influence that frequency has on the system is evident through evaluation of buoy velocity. Taking the case of a Plate acting in Heave, motion at high frequency is seen, in both the experimental videos and numerical results, to limit the vertical velocity of the buoy, attributed here to a system 'lag' where constraint oscillation occurs at a rate greater than can be replicated in system. Considering Morison's equation $F_k = C_d \times A \times \rho \times u^2 \times 0.5$, reduction in buoy velocity will lower the drag force acting as a component of system damping. Restriction to Plate velocity is evident when plotting against extension, as in Figure 26 with *OrcaFlex* data.

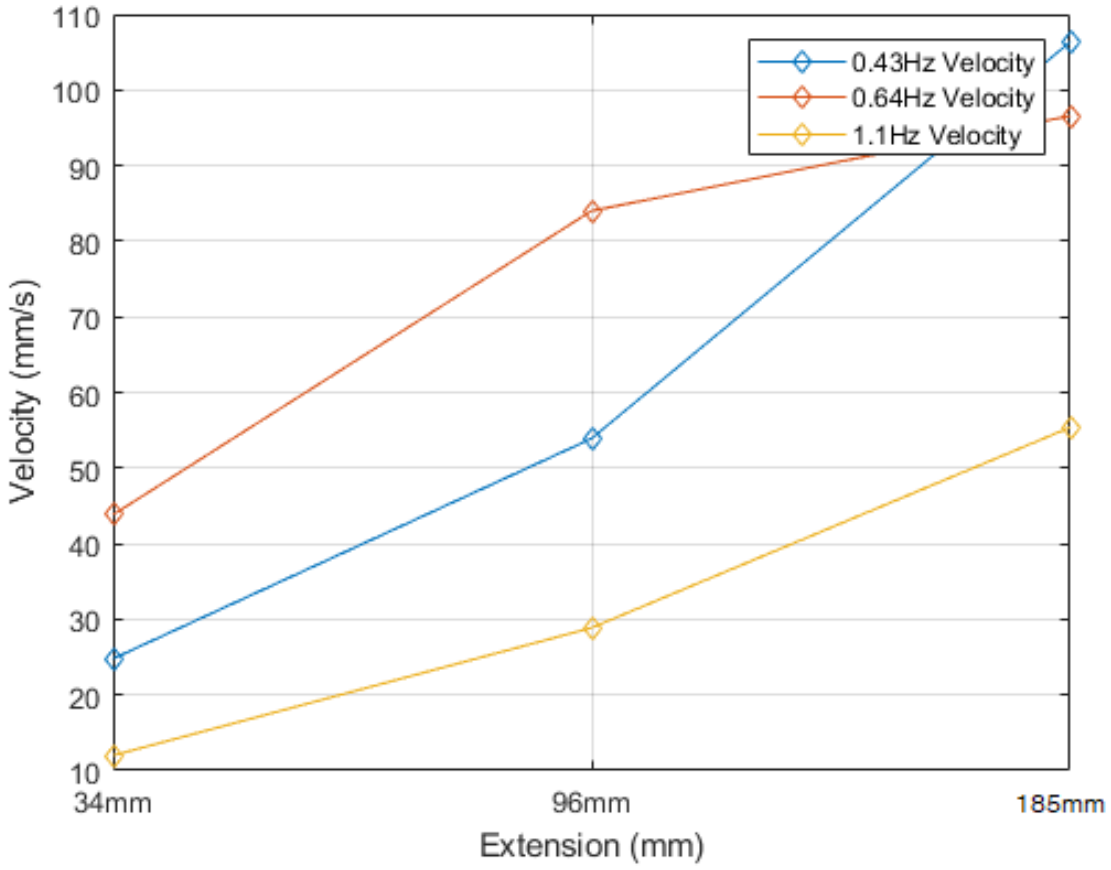

Figure 26: Velocity Influence

Consider a Plate of drag area 5521mm², oscillating in Heave at frequencies of 1.1Hz and 0.64Hz. Using Morison's equation, the calculated drag force and subsequent damping is, as a result, greater for the lower frequency motion than the higher, at 0.155N (1.1Hz) and 0.204N (0.64Hz). Increasing the drag area by 30% at 6773mm² for the Plate oscillating at 1.1Hz, the drag force exerted on the buoy becomes 0.19N – Still a reduction compared to the lower frequency of OWC oscillation, despite the greater surface area. This suggests that as the OWC Heave motion occurs at a

frequency greater than can be replicated in the system, the benefits of increasing drag area reduce.

Limitations and Reliability

The numerical model has limitations principally as a result of scale modelling, and due to necessary approximations of experimental behaviour. Several limitations have been identified below:

- The numerical model is an idealized system, developed through numerical estimation and computational discretization. Consequently, behaviour exhibited by the system during experimentation may not have been replicated – For example, energy losses due to lateral movement of the Heave pulley rig (Roberts, 2020). Load Cell tension fluctuations of 1*10^5 were not accounted for.

- Scale modelling is particularly limited by a lack of catalogue data and requires elements of estimation (Schuring, 1977). In a taut system especially, line and attachment properties may have a significant effect on model dynamics, and scale modelling in *OrcaFlex* may lose modelling intricacies due to inadequate measurement resolution (Paduano, Giorgi & Gomes, 2020). This may explain the lack of resonant behaviour for Heave 0.64Hz. Additionally, variables such as Added Mass were omitted that, while the system seemed insensitive to omission in isolation, may have compounded to influence dynamics.

- Use a sinusoidal wave to excite an OWC for motion is simplified and does not represent in-field spectral conditions, especially due to the omission of wind, waves and currents. As a result, the study findings are not entirely relevant to a full scale OWC nor is a Plate buoy a commonly used geometry for Lazy-S systems. Inclusion of a plate buoy may also have resulted in additional fluid effects effecting dynamics, such as tip vortices. Restriction of the model to Surge and Heave only will also have omitted other 6DOF motions acting on the system.

- The model can predict driving frequency behaviour based on the findings of the *Driving Frequency Amplitude* section. However, due to taut line modelling previously discussed, the model is unable to simulate the numerical tensions of the experimental model. It can therefore not, at its current state, be used for verifying the system against naval architecture installation standards (DNV-GL, 2010), and limits the ability to validate the numerical model against experimental data as tensions may not be equivalent.

Conclusions

To conclude, development and evaluation of a numerical scale model in *OrcaFlex* is a valid methodology, capable of predicting line dynamic behaviour tension trends and the influence of float aspect ratio on driving frequency amplitude. Several conclusions can be made from the numerical findings:

1. Based on the error presented in the *SLF Tension* discussion regarding SLF tension, and evaluation of the standard deviation of tension, modelling of taut scale models may cause numerical discrepancies due to the nodal tension allocation within *OrcaFlex*, and not demonstrate equivalent tension ranges. A mean percentage difference of 11% between MME tension values is adequate for predicting the influence of float geometry on model behaviour, but not be acceptable in terms of analysing a real-world system against standards (DNV-GL, 2010).

2. The effect of increased OWC motion frequency may reduce the influence of the float on system damping. If the OWC is oscillating above 0.64Hz, optimisation of the float will yield diminishing returns when compared to reducing motion frequency. Simply, frequency has a far greater effect on system dynamics than float geometry.

3. Measurement of natural frequency in scale models may suffer as a result of inadequate measurement resolution, such that resonance in Heave 0.64Hz is not measured.

While the results can be applied to a scale model, and predict certain behaviours, significant development is required to allow for the findings to be applied to a full-scale OWC. Further development and recommendations have been provided below.

Future Work

Existing Procedure

Were a new *OrcaFlex* model to be evaluated, several changes could be made to improve the accuracy of results. First, incremental frequency values could be evaluated to determine the resonance behaviour change as a result of property application. In this manner, the difference between the experimental and *OrcaFlex* model could be better quantified. Similarly, additional floats could be introduced to determine their effect on dynamics, rather than plate and spar buoys that may have different fluid flow components as a result of geometry.

Additional Developments

The investigation can be developed further by modelling of a full-scale, three-line OWC allows for application of non-linear environmental spectra, acting as an excitement force. This will improve applicability to real-world systems and allow for better estimation of line properties due to abundant vendor data. OWC hydrodynamic data may be applied, such as radiation diffraction, RAO etc calculations, for a better representation of motion.

A Lazy-S setup with a portion of laydown may be proposed to investigate scale modelling, rather than a taut system that was discovered to contribute to modelling errors. Rather than assessing a complete Lazy-S system, components can be compartmentalised and compared at both full scale and as a scaled prototype. The model may be analysed in all 6 degrees of freedom rather than constrained for a better representation of dynamics.

Ultimately, the effects of scale modelling may be better suited to an independent study rather than a two-tier approach of equivalence to an experimental model, which may better quantify the effect of scale modelling discrepancies. For example, the sensitivity of modal resonance to measurement resolution may be better described by a simplified buoy and line system.

Acknowledgments

I would like to express my deepest thanks to Dr. Keri Collins for her continued support throughout this project, and Senior Technician Paul Smith for providing the OrcaFlex software this work is based on. Finally, I would like to thank George Roberts for providing the experimental model data-set and foundational processing scripts.

Reference List

Ali, M. & Hwa, M. (2020) 'Effects of Water Depth, Mooring Line Diameter and Hydrodynamic Coefficients On The Behaviour Of Deepwater Fpsos'. *Ain Shams Engineering Journal*.

Bingham, H., Ducasse, D., Nielsen, K. & Read, R. (2015) 'Hydrodynamic Analysis of Oscillating Water Column Wave Energy Devices'. *Ocean Eng. Mar. Energy.*

Collins, K., Howey, B. & Greaves, D. (2018) 'D6.5 - Design guidance on the use of shared moorings in compact arrays'.

Davidson, J. & Ringwood, J. (2017) 'Mathematical Modelling of Mooring Systems for Wave Energy Converters—A Review'.

DNV-GL (2010) 'Environmental Conditions and Environmental Loads'. *Det Norske Veritas,* pp. 30 – 40.

Dooley, I. (2020) Modelling Question: UOP Dissertation. Orcina.

Giorgi, G., Gomes, R. & Henriques, J. (2020) 'Detecting Parametric Resonance in a Floating Oscillating Water Column Device for Wave Energy Conversion: Numerical Simulations and Validation with Physical Model Tests'. *Applied Energy 276.*

Grafarend, E. (2006) 'Linear and Nonlinear Models: Fixed Effects, Random Effects, and Mixed Models.' Berlin.

Huse, E. (1991) 'New Developments in Prediction of Mooring System Damping'. *Offshore Technology Conference. Houston: 6th May 1991.*

Kisacik, D., Stratigaki, V. & Wu, M. (2020) 'Efficiency and Survivability of a Floating Oscillating Water Column Wave Energy Converter Moored to the Seabed: An Overview of the EsflOWC MaRINET2 Database'. *MDPI,* pp. 1 – 21.

Lie, H., Gao, Z. & Moan, T. (2007) 'Mooring Line Damping Estimation By A Simplified Dynamic Model '. *26th International Conference on Offshore Mechanics and Arctic Engineering San Diego, California, USA*: 15/10/2007, pp. 197-204.

Liversage, P and Trancossi, M. (2018). 'Analysis of triangular sharkskin profiles according to second law, Modelling, Measurement and Control', pp. 188 - 196.

Martinelli, L. & Zanuttigh, B. (2018) 'Effects of Mooring Compliancy on the Mooring Forces, Power Production, and Dynamics of a Floating Wave Activated Body Energy Converter', pp 1-24.

MIT (n.d.) Linear (Airy) Wave Theory, Available at: http://web.mit.edu/fluidsmodules/www/potential_flows/LecturesHTML/lec19bu/node3.html (Accessed: 01/12/20).

Morison, J. (1950) 'The Force Exerted by Surface Waves on Piles' *J. Pet. Technol,* pp. 149-154.

O'Connell, K., Cashman, A. & Thiebaut, F. (2017) 'Development of a Free Heaving OWC Model with Non-Linear PTO Interaction'. *Renewable Energy 2017.*

Orcina (2020) 6D Buoy Theory, Available at: https://www.orcina.com/webhelp/OrcaFlex/Content/html/6Dbuoytheory,Overview.htm (Accessed: 06/05/21).

Orcina (2020) Attachments: Clumps, Available at: https://www.orcina.com/webhelp/OrcaFlex/Content/html/Attachments,Clumps.htm (Accessed: 25/11/20).

Orcina (2020) Chain: Mechanical Properties, Available at: https://www.orcina.com/webhelp/OrcaFlex/Content/html/Chain,Mechanicalproperties.htm (Accessed: 06/05/21).

Orcina (2020) Line Theory, Available at: https://www.orcina.com/webhelp/OrcaFlex/Content/html/Linetheory,Overview.htm (Accessed: 06/05/21).

Orcina (2020) Resources, Available at: https://www.orcina.com/resources/examples/

Orcina (2020) Static Analysis, Available at: https://www.orcina.com/webhelp/OrcaFlex/Content/html/Staticanalysis.htm (Accessed: 25/11/20).

Orcina (2020) Spectral Response Analysis, Available at: https://www.orcina.com/webhelp/OrcaFlex/Content/html/Chain,Mechanicalproperties.htm (Accessed: 06/05/21).

Paduano, B., Giorgi, G. & Gomes, R. (2020) 'Experimental Validation and Comparison of Numerical Models for the Mooring System of a Floating Wave Energy Converter'. *Journal of Marine Science and Engineering.*

ProteusDS (2019) 'Fiber Rope Cable Properties'. [Online]. Available at: http://documentation.dsaocean.com/tutorials/Tutorials/PDS-AAP.html (Accessed: 05/02).

R.P.F. Gomes, J. C. C. H., L.M.C. Gato, A.F.O. Falcao (2018) 'Time-Domain Simulation Of A Slack-Moored Floating Oscillating Water Column And Validation With Physical Model Tests'. *Renewable Energy, 149*.

Roberts, G. (2020) An Investigation into Mooring Line Dynamics. University of Plymouth.

SamsonRope (2021) 'Amsteel - Blue'. [Online]. Available at: https://samsonrope.com/mooring/amsteel--blue (Accessed: 20/04/2021).

Schuring, D. (1977) "Scale Models in Engineering' Fundamentals and Applications'. Scott, B. (2020) An Investigation into Mooring Line Dynamics. University of Plymouth.

Smith, S. W. (2011) 'Chapter 2: Statistics, Probability and Noise'. The Scientist and Engineer's Guide to Digital Signal Processing. [Online]. Available at: https://www.dspguide.com/ch2/2.htm (Accessed: 05/05/21).

Stappenbelt, B. & Cooper, P. (2010) 'Mechanical Model of a Floating Oscillating Water Column Wave Energy Conversion Device'.

Touzon, I. (2020) 'A Comparison of Numerical Approaches for the Design of Mooring Systems for Wave Energy Converters'. *Journal of Marine Science and Engineering.*

Triantafyllou, M. (1990). 'Cable Mechanics With Marine Applications'; Lecture Notes; Department of Ocean Engineering, Massachusetts Institute of Technology: Cambridge, MA, USA.

Tullow Oil (2019), 'Annual Report.' London, United Kingdom.